Supplementary Information (SI) for Journal of Materials Chemistry A.

Supporting Information

Voltage-driven Surface Reconstruction of Ternary Liquid Metals for Enhanced Electrocatalytic CO_2 Conversion

Chao Li[a, b], *Siwen Guo*[b, f], *Mingjie Li*[b,e*], *Zehui Lin*[a], *Deyu Wang*[c], *Dongming Liu*[d], *Jie Wang*[e], *Xingyun Li*[a, *], *Chaoxu Li*[b, c,*]

[a]Institute of Materials for Energy and Environment, College of Materials Science and Engineering, Qingdao University, Qingdao, 266071 China.

[b]Qingdao Institute of Bioenergy and Bioprocess Technology, Chinese Academy of Sciences, Songling Road 189, Qingdao 266101, P. R. China.

[c]Key Laboratory of Optoelectronic Chemical Materials and Devices of Ministry of Education, Jianghan University, Wuhan 430056, China.

[d]Anhui Province Key Laboratory of Effcient Conversion and Solid-StateStorage of Hydrogen & Electricity, Anhui University of Technology, 243002 Maanshan China.

[e]Key Laboratory of Rubber-Plastics, Ministry of Education/Shandong Provincial Key Laboratory of Rubber-plastics, State Key Laboratory of Advanced Optical Polymer and Manufacturing Technology, Qingdao University of Science & Technology, Zhengzhou Road 53, Qingdao, 266042, P. R. China.

[f]Key Laboratory of Marine Chemistry Theory and Technology (Ministry of Education), College of Chemistry & Chemical Engineering, Ocean University of China, Qingdao 266100, China.

*E-mail: licx@qibebt.ac.cn (C. Li); xingyun_2008@sina.cn (X. Li); limj@qibebt.ac.cn (M. Li).

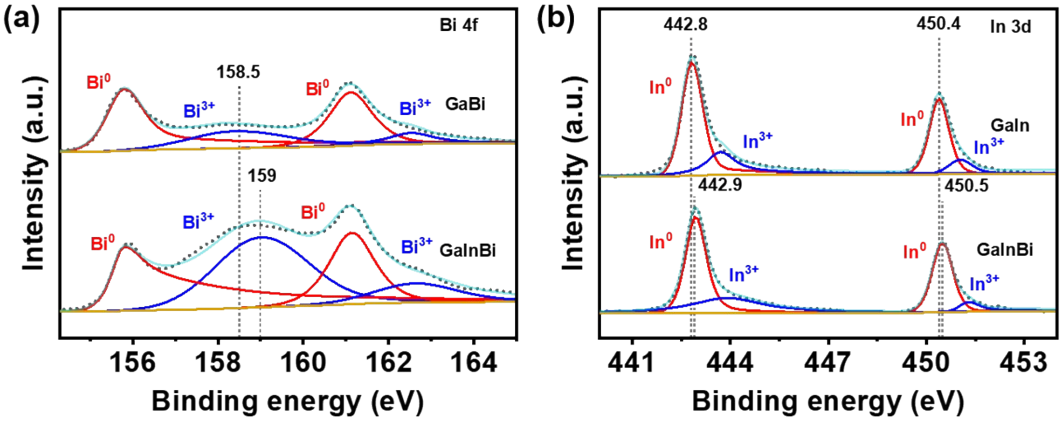

Figure S1. XPS spectra of the Bi (4f) orbital (a) and In (3d) orbital (b) in the liquid alloys $Ga_{83}In_{16}Bi_1$, $Ga_{83}In_{17}$, and $Ga_{99}Bi_1$.

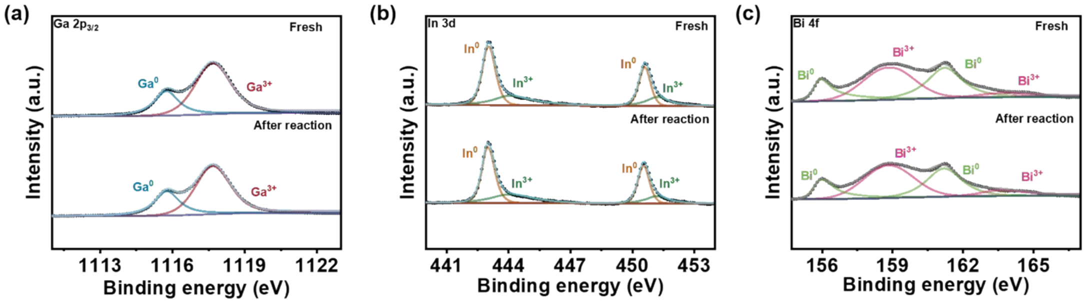

Figure S2. XPS spectra of GaInBi before and after reaction.

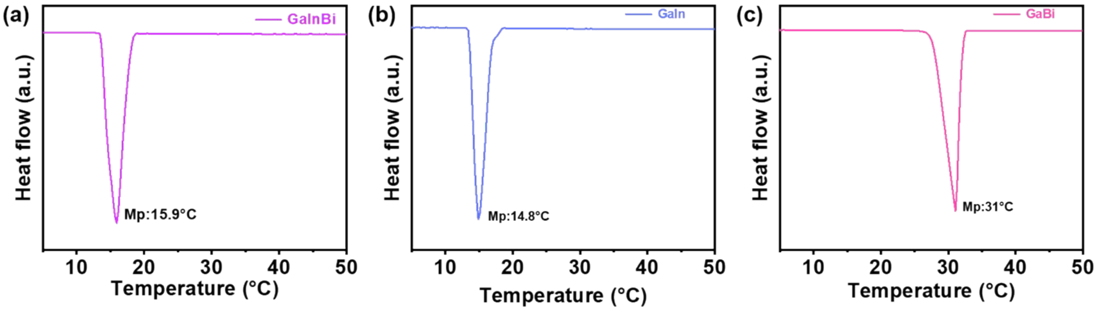

Figure S3. The melting points of GaInBi (a) GaIn, (b) and GaBi (c) determined by differential scanning calorimetry (DSC).

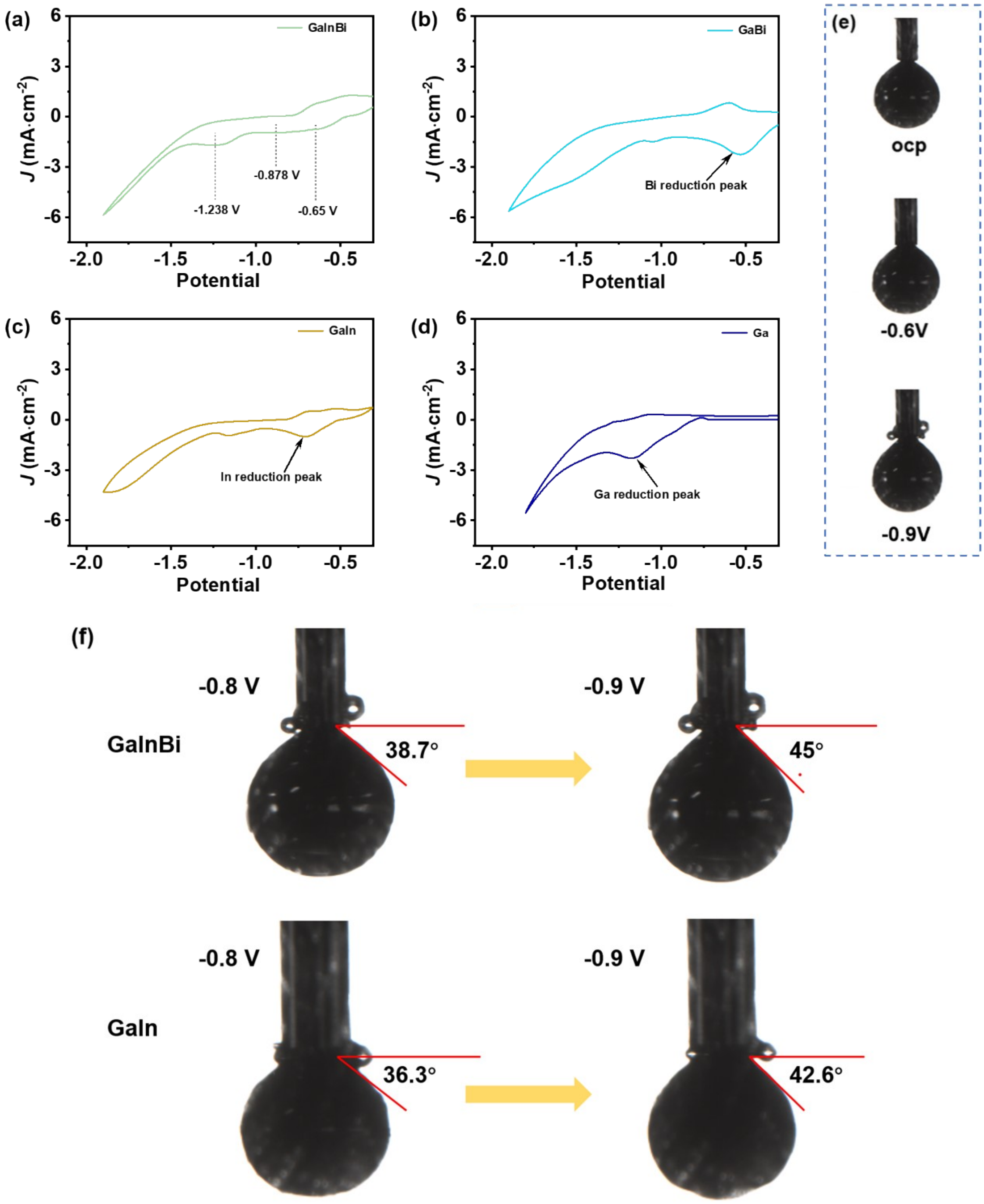

Figure S4. The electrochemical properties of the liquid alloy in 0.3 M EMIMBF$_4$. (V *v.s.* Ag/AgCl) The characteristic cyclic voltammetry curve of (a) GaInBi, (b) GaBi, (c) GaIn and Ga. Sweep rate: 50 mV s^{-1}. (e) The variation of surface tension of GaInBi at different potential. (f) Effect of Cathodic Potential on the Surface Tension of GaInBi and GaIn Alloys.

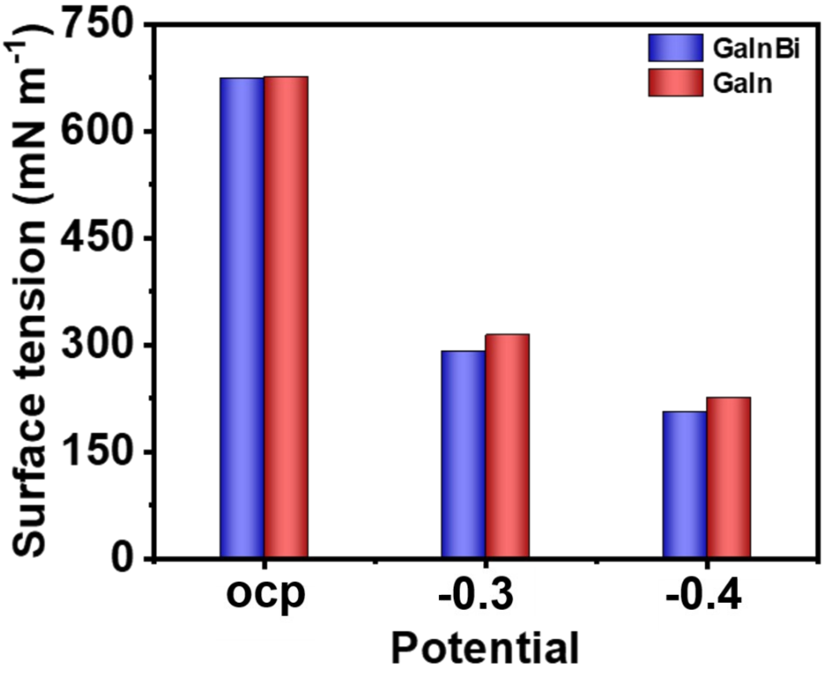

Figure S5. Surface tension variations of GaInBi and GaIn at different cathodic potentials.

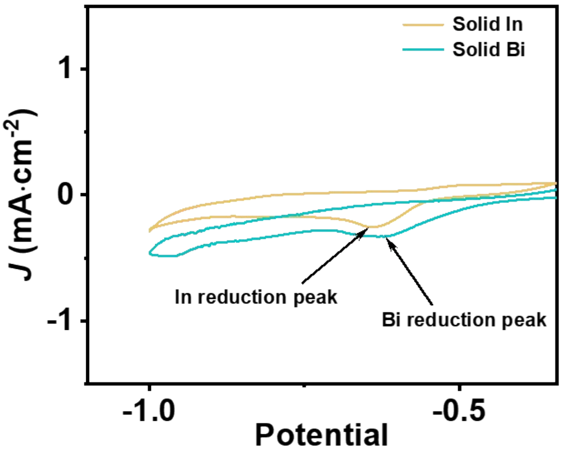

Figure S6. The characteristic cyclic voltammetry curve of Solid In and Solid Bi. Sweep rate: 50 mV s^{-1}, V *v.s.* Ag/AgCl.

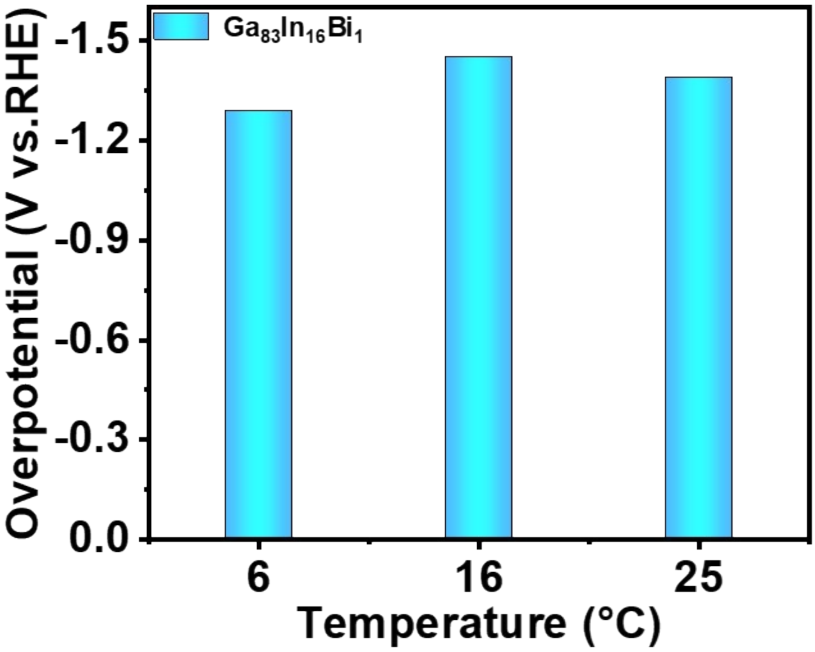

Figure S7. Overpotential of $Ga_{83}In_{16}Bi_1$ at different temperatures. Current density: -2 mA/cm^2.

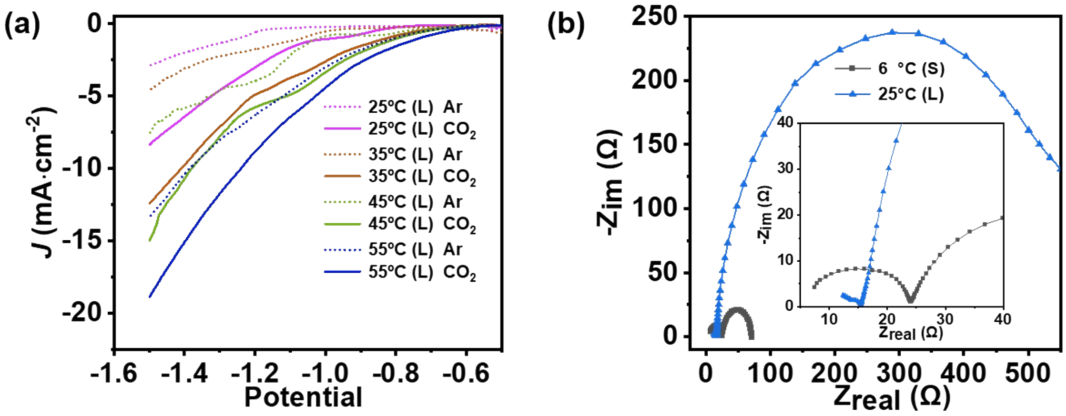

Figure S8. (a) At different temperatures, LSV curves of GaInBi in 0.3 M CO_2 or Ar-saturated $EMIMBF_4$ electrolyte, respectively. (b) Nyquist plots of GaInBi in 0.3 M Ar-saturated $EMIMBF_4$ solution at -1.1 V.

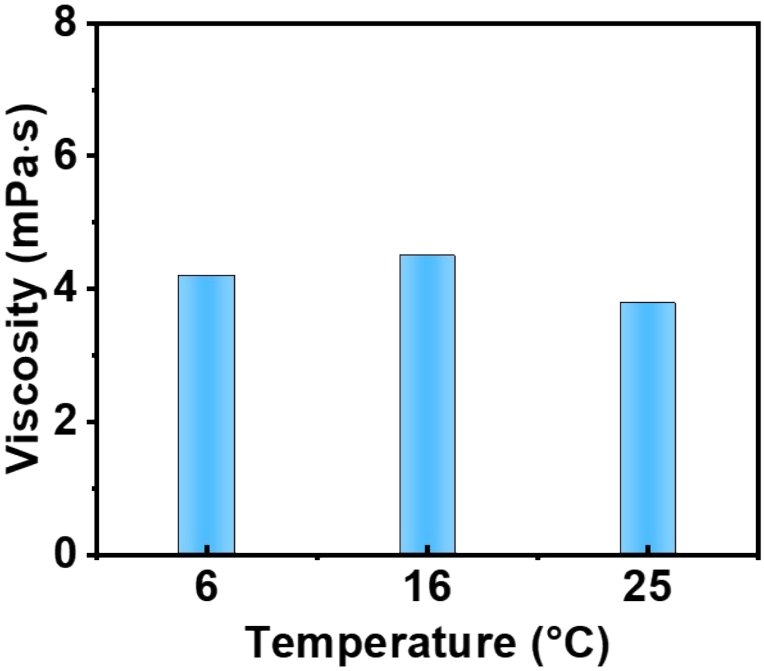

Figure S9. The viscosity of the 0.3 M EMIMBF$_4$ electrolyte at different temperatures.

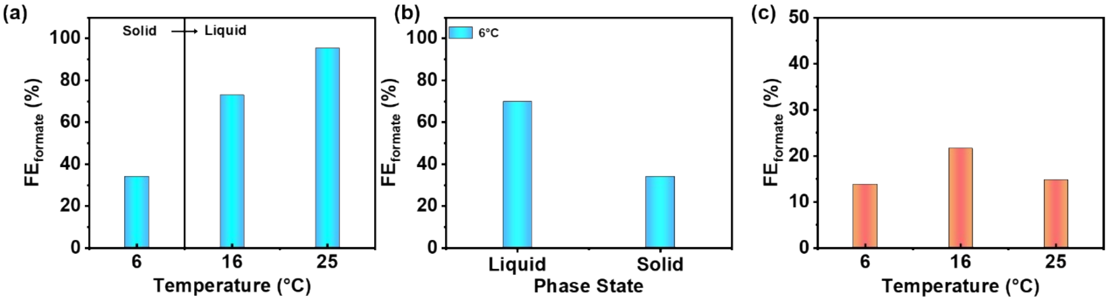

Figure S10. (a) Catalytic performance variation of GaInBi during the solid-to-liquid phase transition at −1.2 V. (b) Comparison of the catalytic performance of GaInBi in the solid and liquid states at −1.2 V. Temperature: 6 °C. (c) Temperature-dependent catalytic performance of solid-state GaBi at −0.9 V.

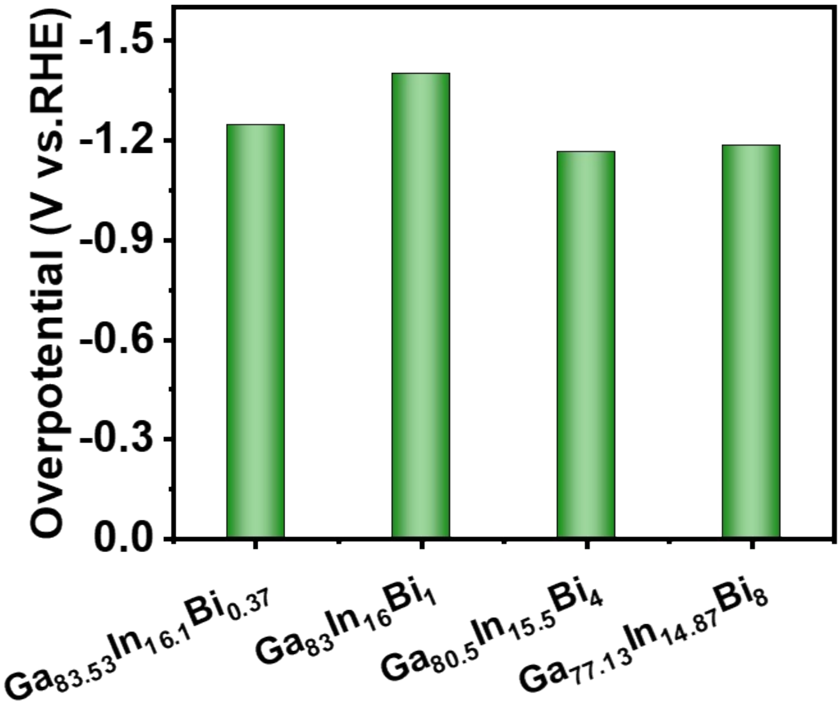

Figure S11. Overpotential at different composition ratios of the alloy. Current density: -2 mA/cm^2.

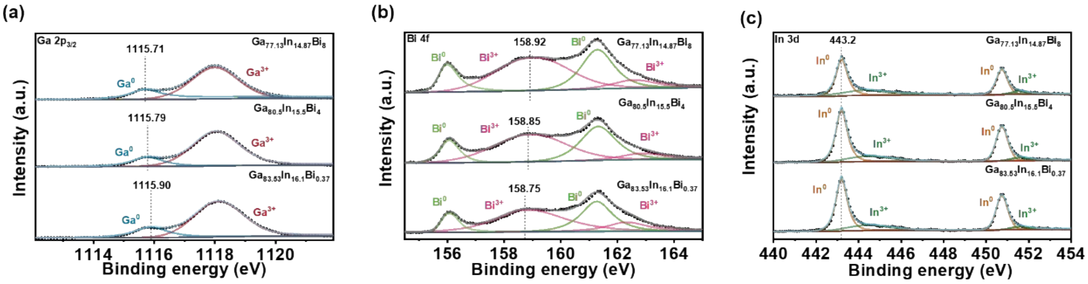

Figure S12. XPS spectra of the Bi (4f) orbital (a) and In (3d) orbital (b) in the liquid alloys $Ga_{77.13}In_{14.87}Bi_8$, $Ga_{80.5}In_{15.5}Bi_4$, and $Ga_{83.53}In_{16.1}Bi_{0.37}$.

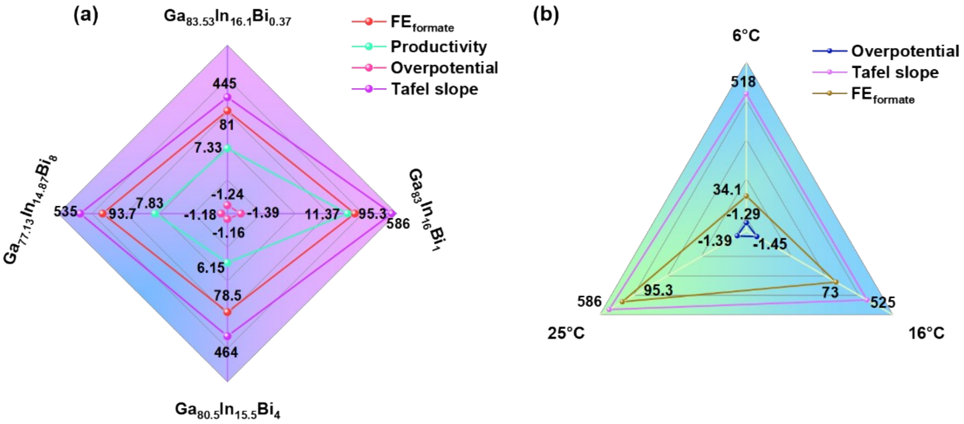

Figure S13. (a) Trend chart of performance characteristics for alloys with different Bi contents. (b) Trend distribution chart of performance characteristics for $Ga_{83}In_{16}Bi_{1}$ at different temperatures. The current density corresponds to the data at -1.2 V *vs.* RHE. The current density corresponding to the overpotential is -2 mA/cm².

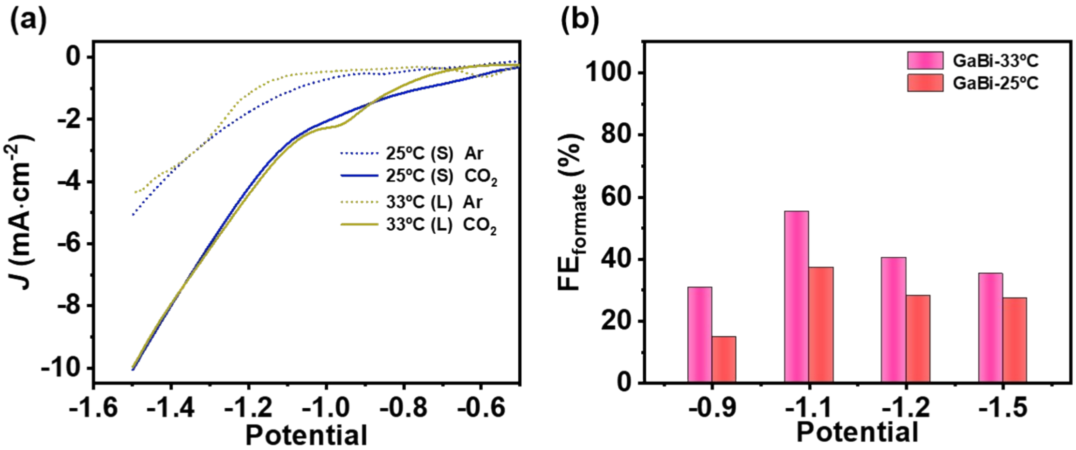

Figure S14. (a) LSV curves of GaBi-25 °C and GaBi-33 °C in 0.3 M CO_2- or Ar-saturated $EMIMBF_4$ electrolyte, respectively. (b) Comparison of the catalytic activity of GaBi-25 °C and GaBi-33 °C at different potentials.

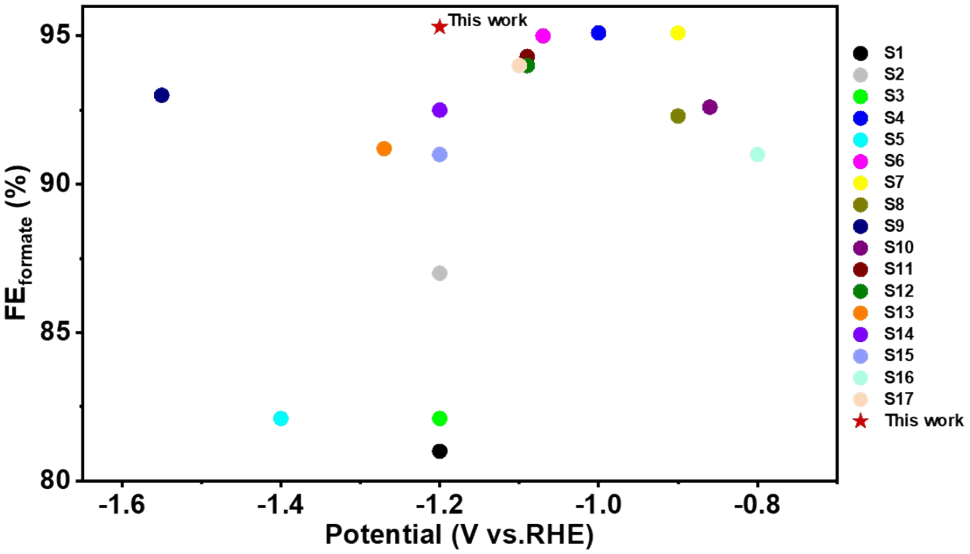

Figure 15. Comparative analysis of catalytic activity with other indium-, bismuth-, and tin-based metals.

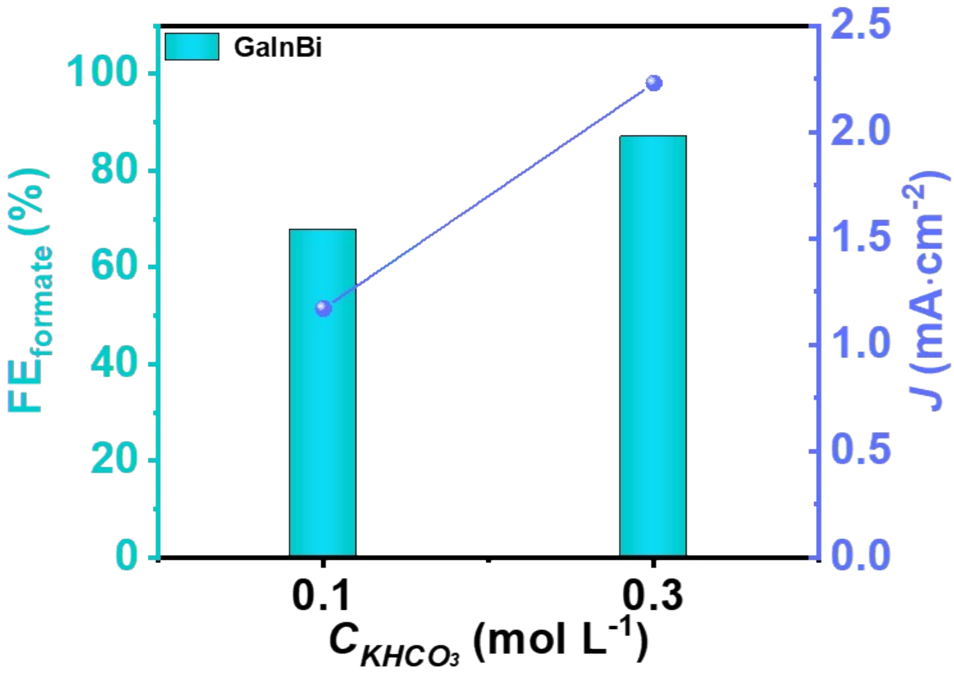

Figure S16. CO_2RR performance in $KHCO_3$ electrolytes at different concentrations.

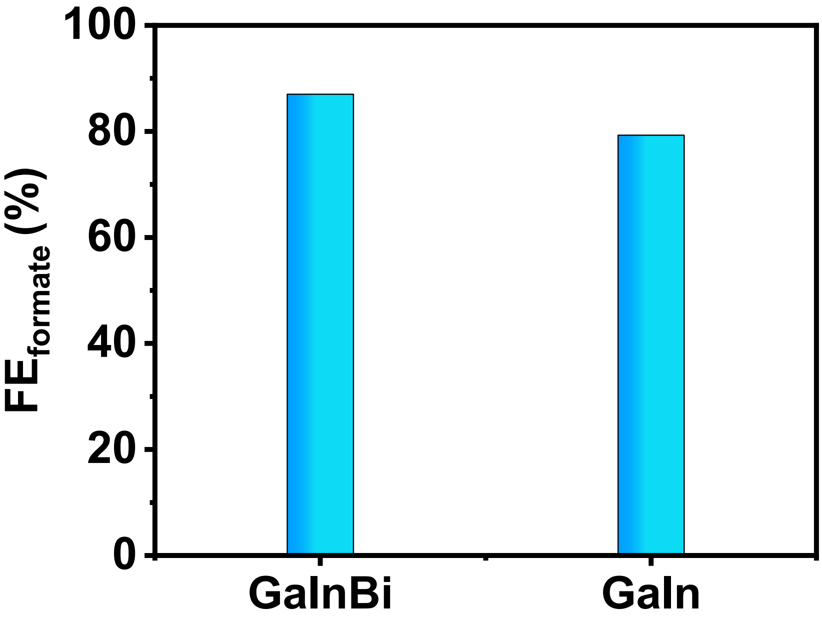

Figure S17. *FE*$_{\text{formate}}$ comparison with GaIn at -1.2 V, 0.3M $KHCO_3$.

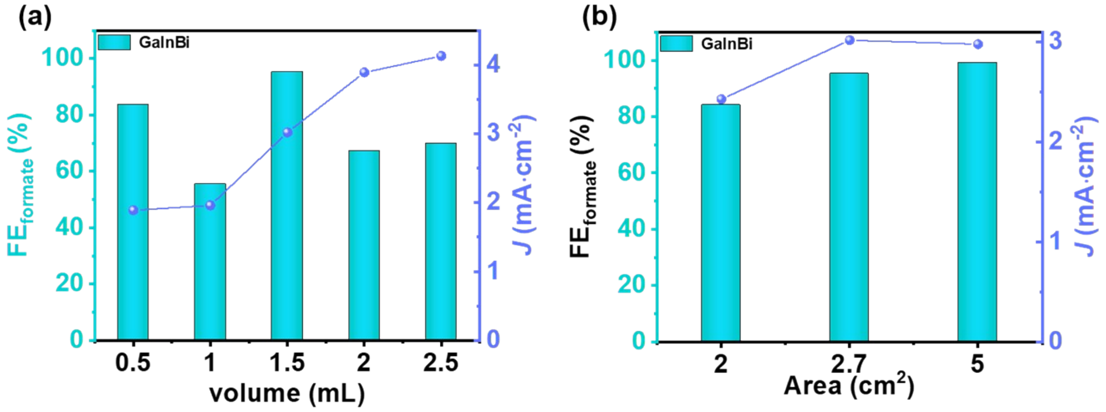

Figure S18. (a) Effect of catalyst volume on performance. (b) The influence of the liquid metal's active surface area on performance.

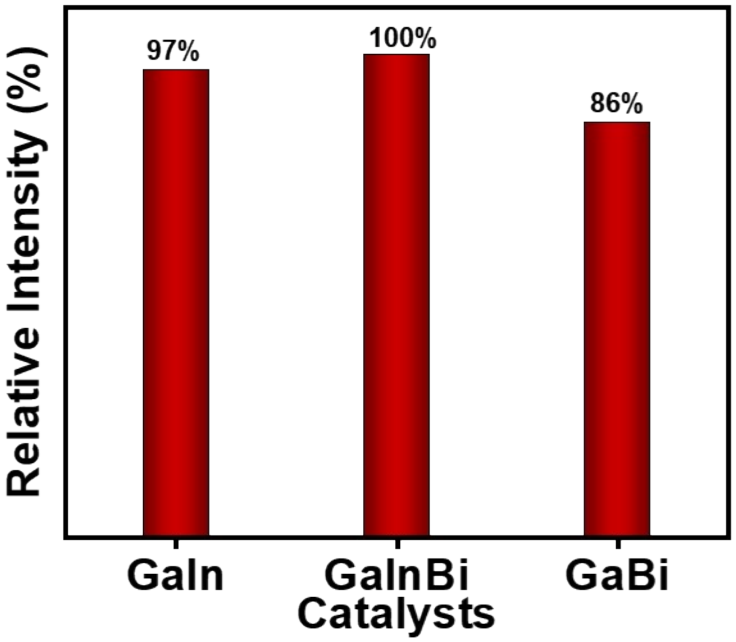

Figure S19. Mass-normalized relative intensity of CO_2 adsorption on GaInBi, GaIn, and GaBi in the high-temperature (above 400 °C) regime.

Figure S20. Optical image of the reaction setup with liquid metal as catalyst.

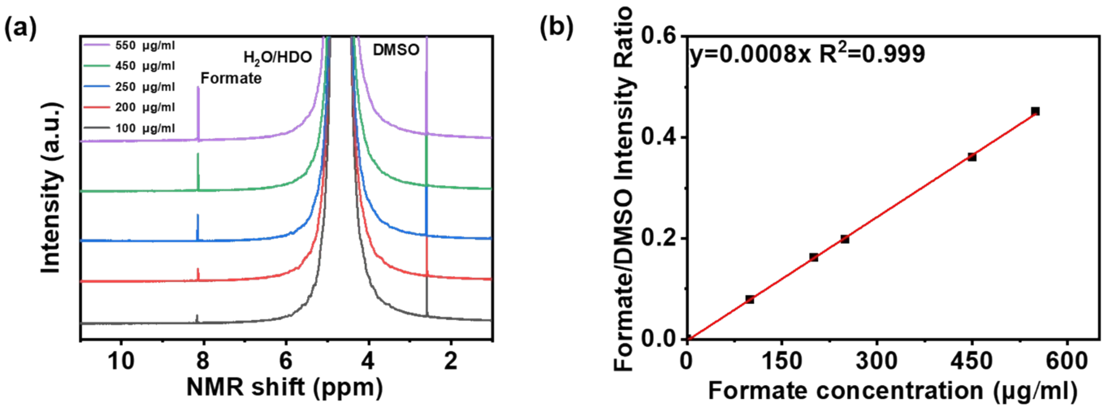

Figure S21. (a) The standard curve is generated from the ^{1}H NMR spectra of formate with known concentrations. (b) The standard curve for quantifying the concentration of formate, the product of CO_2 electrochemical reduction.

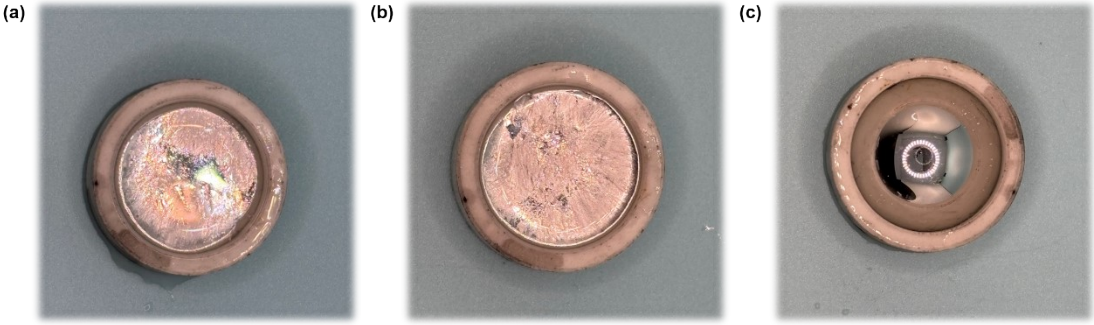

Figure S22. (a) The natural oxidation of the liquid alloy in air forms an oxide layer. (b) The oxide layer formed by applying an anodic potential to the liquid alloy. (c) The removal of the oxide layer by applying a cathodic potential to the liquid alloy.

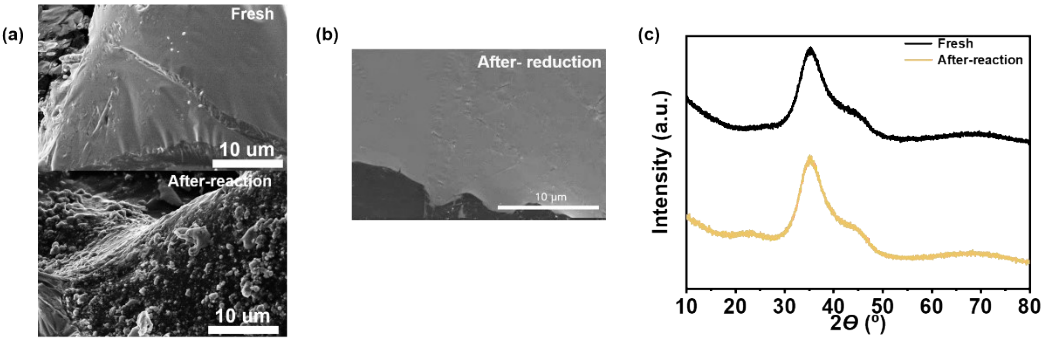

Figure S23. (a) SEM images of the liquid metal before and after reaction. (b) SEM images after electrochemical reduction. (c) XRD pattern characterization of the GaInBi liquid alloy before and after the reaction.

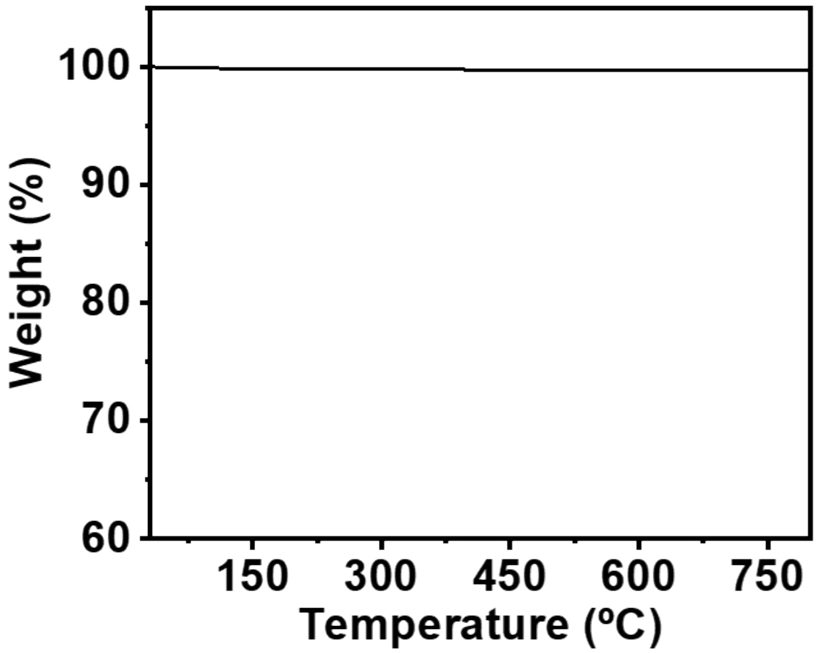

Figure S24. Thermogravimetric analysis (TGA) of the post-reaction liquid metal.

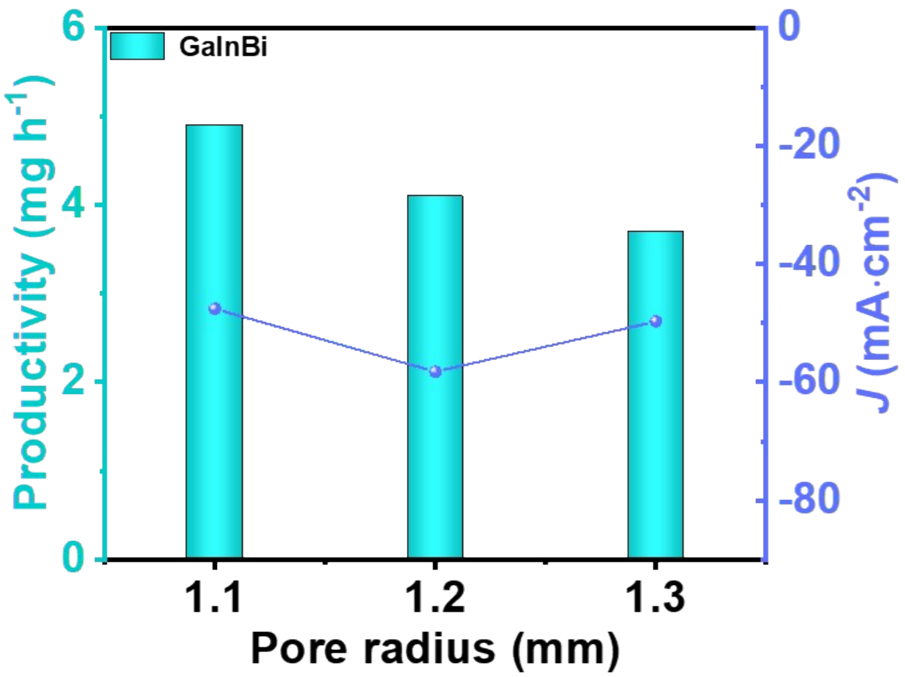

Figure S25. Yield and current density of the liquid metal array electrode at a reaction potential of -1.2 V *vs.* RHE.

Table S1. Changes in the surface elemental composition, as determined by XPS, before and after the reaction.

	Surface element content (wt.%)		
	Ga	**In**	**Bi**
Fresh	87.80	11.00	1.20
Reacted	87.75	11.17	1.08

Table S2. The charge transfer resistances corresponding to the Nyquist plots recorded at -0.9 V and -1.1 V in both Ar-saturated 0.3 M $EMIMBF_4$ solution.

Temperature	**Zreal （Ω）**	**-Zim（Ω）**
6 ℃ (-0.9 V)	713	253
25 ℃ (-0.9 V)	710.9	663.9
6 ℃ (-0.9 V)	23.97	9.439
25 ℃ (-0.9 V)	16.21	2.027
6 ℃ (-1.1 V)	69.47	5.576
25 ℃ (-1.1 V)	72.23	138.4
6 ℃ (-1.1 V)	14.52	8.272
25 ℃ (-1.1 V)	14.28	1.441

Table S3. Performance comparison of indium-, bismuth-, and tin-based catalysts.

Electrocatalyst	**Electrolyte**	**Applied potential (V vs.RHE)**	**FE (%)**	**Ref**
GaInBi	0.3 M $EMIMBF_4$	-1.2	95.3	This work
SnO_x NP-s	0.1 M $KHCO_3$	-1.2	81.0	S1
V, G-SnO_x/C	0.5 M $KHCO_3$	-1.2	87	S2
Pt atom/SnO_2	0.1 M $KHCO_3$	-1.2	82.1	S3
B-SnO_2	0.5 M $KHCO_3$	-1.0	95.1	S4
$CuSn_4$	0.5 M $KHCO_3$	-1.4	82.1	S5
CeOx-Sn	1.0 M KOH	-1.07	95	S6
$SnSe_2$-graphene	0.1 M $KHCO_3$	-0.9	95.1	S7
Bi-NFs	0.1 M $KHCO_3$	-0.9	92.3	S8
BOC-NS	1.0 M KOH	-1.55	93	S9
CDB	1.0 M KOH	-0.86	92.6	S10
Bi_2O_3/p-rGO	0.1 M $KHCO_3$	-1.09	94.3	S11
Bi/CNFs-900	1.0 M KCl	-1.09	94	S12

R-In_2O_3	0.1 M $KHCO_3$	-1.27	91.2	S13
F-$In(OH)_3$	0.1 M $KHCO_3$	-1.2	92.5	S14
In_2S_3-RGO	0.1 M $KHCO_3$	-1.2	91	S15
mp-In@MWCNTs	0.1 M $KHCO_3$	-0.8	91	S16
MIL-68(In)-NH_2	1.0 M $KHCO_3$	-1.1	94	S17

Table S4. Comparison of electrochemical parameters for different CO_2 reduction systems towards formate production.

Electrocatalyst	**Electrolyte**	**Applied potential (V vs.RHE)**	**FE (%)**	**Tafel slope（mV/dec）**	**Current density (mA/cm^2)**	**Ref**
GaInBi	0.3 M $EMIMBF_4$	-1.2	95.3	586	4.85	This work
Pt atom/SnO_2	0.1 M $KHCO_3$	-1.2	82.1	/	7.8	S3
B-SnO_2	0.5 M $KHCO_3$	-1	95.1	145	42.35	S4
$CuSn_4$	0.5 M $KHCO_3$	-1.4	82.1	/	150	S5
F-$In(OH)_3$	0.1 M $KHCO_3$	-1.2	92.5	/	5.5	S14
In_2S_3-RGO	0.1 M $KHCO_3$	-1.2	91	142	10.9	S15
mp-In@MWCNTs	0.1 M $KHCO_3$	-0.8	91	134	78.5	S16
MIL-68(In)-NH_2	1.0 M $KHCO_3$	-1.1	94	176	108	S17
Cu-SnO_2	0.5 M $KHCO_3$	-0.9	90	224	220	S18
$PdC_{0.13}$/CNT	0.5 M K_2SO_4	-0.9	95	535.3	1000	S19
$Pd_1Cu_{0.3}$	1.5 M $KHCO_3$	-0.8	90	/	150	S20

REFERENCES

S1 Kim, M.; Lee, H.; Won, J., et al. Design of less than 1 nm scale spaces on SnO_2 nanoparticles for high-performance electrochemical CO_2 reduction. *Adv. Funct. Mater*. 2022, **32**, 2107349.

S2 Wei, X.; Li, Z.; Jang, H., et al. Synergistic effect of grain boundaries and oxygen vacancies on enhanced selectivity for electrocatalytic CO_2 reduction. *Small*. 2024, **20**, 2311136.

S3 Zhou, X.; Song, E.; Kuang, Z.; Gao, Z.; Zhao, H.; Liu, J.; Sun, S.; Mou, C.; Chen, H. Tuning selectivity of electrochemical reduction reaction of CO_2 by atomically dispersed Pt into SnO_2 nanoparticles. *Chem. Eng. J*. 2022, **430**, 133035.

S4 S4 Zhong, X.; Yang, T.; Liang, S.; Zhong, Z.; Deng, H. Boron dopant modulated electron localization of tin oxide for efficient electrochemical CO_2 reduction to formate. *Small*. 2023, **19**, 2303185.

S5 Li, D.; Xie, S.; Liang, J.; Ma, B.; Fu, J.; Wu, J.; Feng, Y.; Feng. Z. Structure regulated CuSn alloy catalyst for selective electrochemical CO_2-to-formate conversion at higher current densities. *Sep. Purif. Technol*. 2024, **340**, 126545.

S6 Zhu, Y.; Sun, X.; Zhang, R.; Feng, X.; Zhu, Y. Interfacial electronic interaction in amorphous-crystalline CeO_x-Sn heterostructures for optimizing CO_2 to formate conversion. *Small*. 2024, **20**, 2400191.

S7 Shao, S.; Wen, T.; Wang, Z.; Yin, X.; Liu, Y.; Yang, W.; Chen, Y. Fabrication of $SnSe_2$-graphene nanosheets for highly effectively electrocatalytic reduction of CO_2. *Electrochim. Acta*. 2022, **434**, 141331.

S8 Yang, S.; Jiang, M.; Zhang, W.; Hu, Y.; Liang, J.; Wang, Y.; Tie, Z.; Jin, Z. *In situ* structure refactoring of bismuth nanoflowers for highly selective electrochemical reduction of CO_2 to formate. *Adv. Funct. Mater*. 2023, **33**, 2301984.

S9 Fan, T.; Ma, W.; Xie, M., et al. Achieving high current density for electrocatalytic reduction of CO_2 to formate on bismuth-based catalysts. *Cell Rep. Phys. Sci*. 2021, **2**, 100353.

S10 Shen, H.; Zhao, Y.; Zhang, L.; He, Y.; Yang, S.; Wang, T.; Cao, Y.; Guo, Y.; Zhang, Q.; Zhang. H. *In-situ* constructuring of copper-doped bismuth catalyst for highly efficient CO_2 electrolysis to formate in ampere-level. *Adv. Energy Mater*. 2023, **13**, 2202818.

S11 Kou, X.; Zhang, Y.; Niu, D.; Han, X.; Ma, L.; Xu. J. Polyethylene oxide-engineered graphene with rich mesopores anchoring Bi_2O_3 nanoparticles for boosting CO_2 electroreduction to formate. *Electrochim Acta*. 2022, **433**, 141256.

S12 Kong, Y.; Jiang, X.; Li, X.; Sun, J.; Hu, Q.; Chai, X.; Yang, H.; He. C. Boosting electrocatalytic CO_2 reduction to formate *via* carbon nanofiber encapsulated bismuth nanoparticles with ultrahigh mass activity. *Chinese J Catal*. 2023, **45**, 95.

S13 Cheng, Q.; Huang, M.; Xiao, L., et al. Unraveling the influence of oxygen vacancy concentration on electrocatalytic CO_2 reduction to formate over indium oxide catalysts. *ACS Catal.* 2023, **13**, 4021.

S14 An, X.; Li, S.; Yang, Z., et al. F-doped $In(OH)_3$ for electrochemical reduction of CO_2 to formate. *Chem. Eng. J*. 2023, **455**, 140720.

S15 Ning, H.; Fei, X.; Tan, Z.; Wang, W.; Yang, Z.; Wu. M. *In situ*-fabricated In_2S_3-

reduced graphene oxide nanosheet composites for enhanced CO_2 electroreduction to formate. *ACS Appl. Nano Mater*. 2022, **5**, 2335.

S16 Xiao, L.; Zhou, R.; Zhang, T.; Wang, X.; Zhou, R.; Cullen, P.; Ostrikov, K. Porous indium nanocrystals on conductive carbon nanotube networks for high-performance CO_2-to-formate electrocatalytic conversion. *Energy Environ. Mater*. 2024, **7**, e12656.

S17 Wang, Z.; Zhou, Y.; Xia, C.; Guo, W.; You, B.; Xia, B. Efficient electroconversion of carbon dioxide to formate by a reconstructed amino-functionalized indium-organic framework electrocatalyst. *Angew. Chem. Int. Edit*. 2021, **60**, 19107.

S18 Li, B.; Chen, J.; Wang, L., et al. Dynamic reconstruction of Cu-doped SnO_2 for efficient electrochemical reduction of CO_2 to formate. *Appl. Catal., B*. 2025, **363**, 124784.

S19 Yu, Y.; Wang, Z.; Wang, W., et al. Small PdC_x interstitial compound for efficient acidic CO_2 electroreduction to formic acid. *Nat. Commun*. 2026, **17**, 1181.

S20 Lv, X.; Luo, T.; Lv, C., et al. Bicarbonate-dependence for Pd-catalyzed CO2 hydrogenation to formate over an electronegativity-induced bimetallic center. *J. Am. Chem. Soc*. 2025, **147**, 42194-42208.